57th 3AF International Conference on Applied Aerodynamics
29 – 31 March 2023, Bordeaux - France

AERO2023-69

Numerical Investigation of the Influence of Acceleration and Deceleration on the Aerodynamic Characteristics of an Oscillating Wing Aerofoil Operating at Transonic and Hypersonic Speeds

Shine Win Naung[1*], Mohmmad Rahmati[1], Laurent Dala[1]
[1]Department of Mechanical and Construction Engineering, Northumbria University, Newcastle upon Tyne, NE 1 8ST, United Kingdom, [*]Email: shine.w.naung@northumbria.ac.uk

ABSTRACT

The aerodynamic characteristics of a hypersonic aircraft are strongly influenced by the accelerating and decelerating motions of the body. This impact can be more complicated when the oscillatory motion of the body in a complex non-linear mode is involved. Therefore, it is important to understand the mechanism of the responses of the body to acceleration and deceleration at different magnitudes. This paper uses a Computational Fluid Dynamics (CFD) method to investigate the mechanism of acceleration and deceleration at three different magnitudes such as 100g, 1000g and 10000g, and their effects on the aerodynamic characteristics and performance of an oscillating blunt body, which represents the leading edge of a wing aerofoil of a hypersonic aircraft operating at transonic and hypersonic speeds ranging from M = 2 to M = 8. It is revealed that the low Mach numbers have more impact on the aerodynamic performance of the body. The results of the 100g and 1000g acceleration or deceleration magnitudes are in close agreement while that of the 10000g are slightly lower or higher during acceleration or deceleration, respectively. The boundary of the shock wave becomes narrower and the distance of the shock wave from the nose of the body gets shorter as the Mach number is increased, whereas the fluid velocity recovers quickly in the boundary layer at low Mach numbers.

1. INTRODUCTION

There is a growing number of engineering applications, in which the effects of acceleration and deceleration are dominant, such as aeronautical vehicles. It can be considered that the acceleration and deceleration of an object is a combined effect of both translational and rotational motions in a frame of reference [1, 2]. High magnitudes of acceleration and deceleration are deemed necessary in some applications such as projectiles or manoeuvring planes. A re-entry vehicle entering the atmosphere often encounters acceleration and deceleration with a high amplitude [3]. Aircrafts operating at supersonic speeds also experience acceleration and deceleration, which has a great influence on the viscous boundary layer of the wings [4]. The near-wall characteristics of the surface are affected by acceleration and deceleration effects, and as a result, the pressure and velocity distribution over the wing surface is greatly altered. In addition, a wing of hypersonic aircraft may encounter vibration at a small amplitude during the acceleration and deceleration process. An oscillatory motion of the wing adds additional flow disturbances and aggravates the situation. An extensive investigation of the response of the boundary layer to acceleration and deceleration effects is required for the design and concurrent optimisation procedure of hypersonic aircraft wings [5].

Gledhill et al. [6] highlighted that the accelerating motion reduces the drag by approximately 20% in the transonic flow regime. A numerical study by Roohani et al. [7] demonstrated the impact of acceleration and deceleration on the development of shockwave and aerodynamic loads at transonic speeds. The effects of acceleration and deceleration on unsteady aerodynamic characteristics of a train were also investigated by Niu et al. [8], and it was found that the train experienced a strong unsteady flow phenomenon during the process of acceleration and deceleration, which influenced the aerodynamic parameters of the train.

Various experiments have been designed and proposed to investigate the effects of accelerating and decelerating motions of different objects. A wind tunnel experiment to analyse the effects of acceleration of a cylinder was conducted in the study of Shirato et al. [9]. Likewise, Yang et al. [10] also performed a wind tunnel test to investigate the response of a

cylinder object to acceleration. In these experiments, the speed and frequency of the fan of the wind tunnel were varied to have the desired Reynolds number and the magnitude of acceleration or deceleration. Furthermore, the impact of acceleration on the lift applied on the wings of a forward flight was investigated in the experiments of Sawyer et al. [11, 12]. However, it was argued that wind tunnel experiments cannot accurately reproduce the behaviour of an object experiencing acceleration and/or deceleration at high speeds [13].

With the technical advances in computing technology, Computational Fluid Dynamics (CFD) methods have been widely used in the aerospace industry due to the advantages of providing flow details and accuracy in predicting aerodynamic characteristics depending on appropriate turbulence modelling. Win Naung et al. [14] performed high-fidelity CFD studies to analyse the interaction between the transient flow and the oscillating blades in a modern low-pressure turbine of an aero-engine. They also investigated the effects of Reynolds numbers, based on an inflow speed, on the transitional and turbulence flow structures around oscillating blades and highlighted that high-fidelity CFD methods are required to accurately predict the unsteady flow behaviour [15].

Different numerical methods have been developed to model the acceleration and deceleration of an object. Moving mesh and moving frame of reference methods are typically applied to the modelling of acceleration and deceleration of objects. A sliding mesh method was proposed by Steijl et al. [16] to investigate the relative motion between the blades of the rotor and the fuselage of a helicopter. Inoue et al. [17] employed a moving cell method to numerically analyse the unsteady flow and the shock wave introduced by accelerating motions. Similarly, Marquart et al. [18] developed a moving mesh method to evaluate unsteady aerodynamic loads over an accelerating aerofoil. The effect of decelerating sphere on the shock distance was analysed by Saito et al. [19] using a fixed coordinate system. Li et al. [20] developed the formulation for the modelling of a cylinder experiencing forced and free motions based on a moving grid method. The moving frame of reference, on the other hand, requires the formulation of the governing equations in a non-inertia reference frame. Refs [21, 22] considered the continuity and the conservation of momentum equations to study steady rotational motions, whereas [23, 24] modelled coupled unsteady rotational and translational motions. Moreover, Combrinck et al. [25] derived the continuity equation, and the conservation of momentum and energy equations to model the combined unsteady rotation and translation motions of an accelerating object.
The overarching aim of this paper is to numerically investigate the response of the boundary layer of an oscillating wing operating at transonic and hypersonic speeds to the acceleration and deceleration effects. The influence of the combined effects of acceleration/deceleration and the aerofoil oscillation on the development of the aerodynamic characteristics of the wing will be explored using a CFD method. A hypersonic blunt aerofoil body will be employed for the modelling of the wing in this analysis. The bending mode of the wing will be integrated into the flow simulations to initiate the oscillatory motion of the wing aerofoil. The unsteady aerodynamic flow behaviours will be extensively investigated in the present study. Unsteady aerodynamic simulations will be performed using the commercial software ANSYS Fluent 2022R1. Acceleration and deceleration simulations of the wing will be performed at transonic and hypersonic speeds in the range of M = 2 to M = 8 based on an oscillating wing aerofoil. Initially, the aerofoil will operate at a constant speed in a steady-state condition before acceleration or deceleration is applied. This numerical approach can also be utilised for the design and analysis of other applications such as high-speed trains.

2. PHYSICAL AND COMPUTATIONAL DESCRIPTIONS

2.1. Physical Description

In this paper, a blunt body is employed as a section of a wing model and it undergoes linear acceleration and deceleration in the numerical simulations. The model was adopted from one of the most cited benchmark models operating in the hypersonic flow regime. As seen in Fig. 1, the model has a cylindrical shape nose, which can also be considered as a leading edge of a wing aerofoil. The flow conditions and the design parameters of the blunt body are presented in Table 1. The blunt body is initially operating at a steady Mach number before acceleration or deceleration is applied (i.e., M = 2 in the case of acceleration and M = 8 in the case of deceleration). In this study, three different magnitudes of acceleration and deceleration such as 100g, 1000g and 10000g where g is the gravity ($g = 9.81\ ms^{-1}$) are considered in this study. In the case of acceleration, the Mach is raised from M = 2 up to M = 8 at a given rate of magnitude, and the process is reversed in the case of deceleration. Furthermore, an oscillation of the body is also considered in this study to investigate the effects of oscillation of the blunt body during the acceleration or deceleration process.

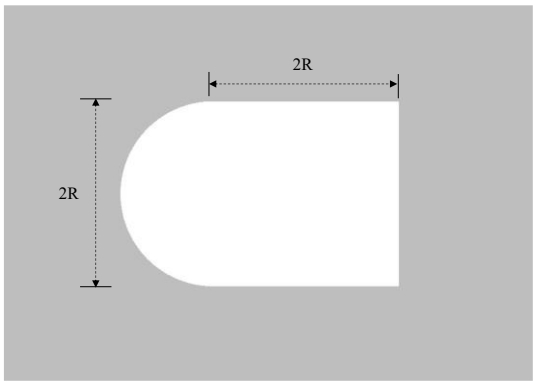

Figure 1. Geometry of the blunt body.

Table 1. Freestream parameters.

Parameters	Value
Mach number	2 - 8
Freestream pressure [Pa]	855
Freestream temperature [K]	125.07
Wall temperature [K]	294
Blunt body radius, R [m]	0.0381

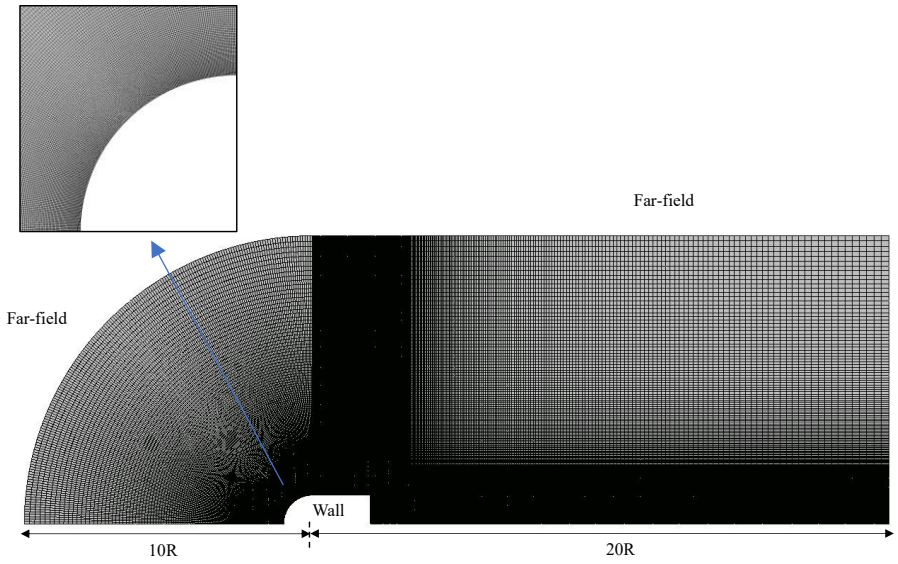

Figure 2. Computational domain and mesh.

2.2. Computational Domain and Mesh

Figure 2 shows the computational domain created for the intended simulations to investigate the aerodynamic characteristics of the blunt body operating at transonic and hypersonic flows and experiencing acceleration or deceleration. The far-field boundary is located 10R from the origin of coordinates, whereas the outflow area is placed 20R from the origin in the downstream region, where R is the radius of the blunt body, to ensure the far-field boundaries are far enough from the body so as not to affect the flow around the body. A hexahedral structured grid is generated over the entire domain as shown in Fig. 2. To sufficiently resolve the boundary layer, the near-wall resolution y^+ is kept lower than 1 over the surface of the body. A mesh sensitivity study is also carried out (which will be discussed in the next section) to ensure that the generated grid is appropriate for the simulations discussed in this paper.

2.3. Numerical Scheme

A three-dimensional, density-based, finite volume solver is used to solve the flow governing equations, and the Navier-Stokes equations can be expressed as [14, 15]:

$$\frac{\partial}{\partial t}\int_Q UdQ + \int_A \vec{F}_I \,.\, d\vec{A} + \int_A \vec{F}_V \,.\, d\vec{A} = \int_\Omega SdQ \qquad (1)$$

where Q is the computational volume, A is the surface, U is the conservative flow variables, S is the source term, and $\vec{F}_I$ and $\vec{F}_V$ are the inviscid and viscous flux, respectively. An Unsteady Reynolds Averaged Navier-Stokes (URANS) model is employed, and a standard k-omega SST model is used as a turbulence model in this study. The flow governing equation can be written in a semi-discrete form as follow:

$$\frac{\partial}{\partial t}(U) = R(U) \tag{2}$$

where R is the lumped residual and source term. A pressure far-field boundary is applied on the far-field or external boundaries as shown in Fig. 2, and a no-slip wall boundary is defined on the blunt body. A Mach number and a freestream pressure and temperature are specified for the pressure far-field boundary.

To integrate the oscillation of the blunt body, the translational displacement is specified on the wall boundary as follows [26-28]:

$$d(t) = \bar{d} + d_A \sin(\omega t) \tag{3}$$

where $\bar{d}$ and d_A are the time-averaged value and amplitude of the oscillation of the blunt body. The unsteady flow variables can be expressed by the Fourier series for a specified frequency, ω, and specific harmonic numbers (m), as shown in Eq. 4.

$$U = \bar{U} + \sum_{m=1}^{M} [U_A \sin(m\omega t) + U_B \cos(m\omega t)] \tag{4}$$

where U, U_A and U_B are the Fourier coefficients of the unsteady flow variables, and ω is the frequency of the oscillation of the body. Substituting the above decomposition into the semi-discrete form of the governing equations yields:

$$\omega \sum_{m=1}^{M} [mU_A \cos(m\omega t) - mU_B \sin(m\omega t)] = R \tag{5}$$

Unsteady compressible flows are solved based on a coupled implicit formulation. A second-order upwind scheme is used for the spatial discretisation and a dual time-stepping method is used for the temporal discretisation. A least square cell-based method is used for the computation of gradients and Roe-FDS is employed for the processing of flux type. The residuals for the conservation of mass and momentum equations are set to 10^{-4}, whereas it is set to 10^{-6} for the energy equation to ensure the solution convergence.

3. RESULTS AND DISCUSSION

Before analysing further, it is important to verify and validate the employed numerical model to make sure that the model is accurate and reliable. A mesh sensitivity study is first carried out to select the optimum mesh size. Figure 3 plots the averaged force applied on the surface body with respect to the number of elements generated for different mesh sizes. It can be seen that there is no significant improvement in the prediction after 100,000 elements. The selected mesh is comprised of 115,344 elements. After having obtained confidence in the mesh, the accuracy of the model is then tested against a benchmark test. Both experimental and numerical data are available, and the pressure coefficient distribution along the cylindrical nose of the blunt body computed from the present analysis is compared to those of the experiment [29] and a reference simulation [30] (see Figure 4). It is seen that a good agreement is obtained between the present simulation and the experiment, and the results are also in close agreement with the reference simulation available in the literature. Therefore, it is concluded that the numerical model employed in the present analysis is both reliable and accurate.

Steady-state simulations are initially performed at M = 2 and M = 8, and they are defined as the initial condition in the unsteady simulation when acceleration or deceleration magnitudes are applied. In the case of acceleration, the blunt body accelerates from M = 2 up to M = 8 at a given magnitude, and on the other hand, the body decelerates from M = 8 to M = 2 in the case of deceleration. Figure 5 compares the dimensionless pressure, normalised by the freestream pressure, averaged over the surface of the blunt body for different magnitudes during the acceleration process. For better analysis, it is divided into two charts: one for low Mach numbers (M = 3 to M = 5) and the other one for high Mach numbers (M = 6 to M =8). It is found that almost no difference is seen between the magnitudes of 100g and 1000g, whereas a noticeable difference is observed when the magnitude is increased to 10000g. The difference is more pronounced at lower Mach numbers when the body starts to accelerate. At all Mach numbers, the pressure distribution on the body at the acceleration magnitude of 10000g is slightly lower than that of 100g and 1000g.

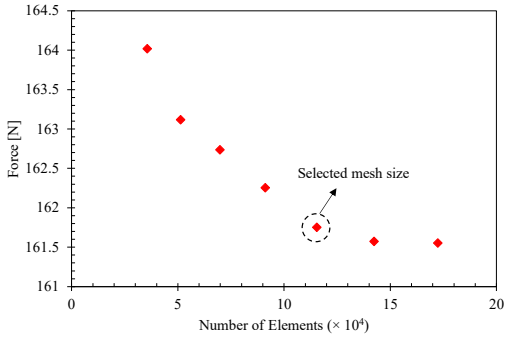

Figure 3. Mesh sensitivity study.

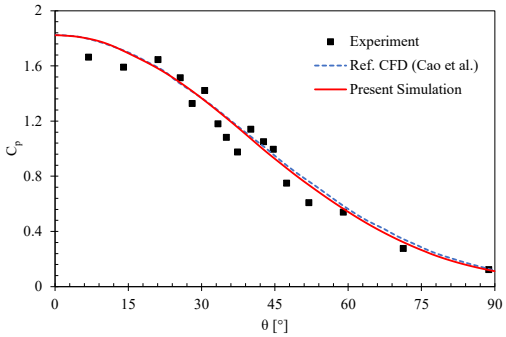

Figure 4. Validation of the CFD model.

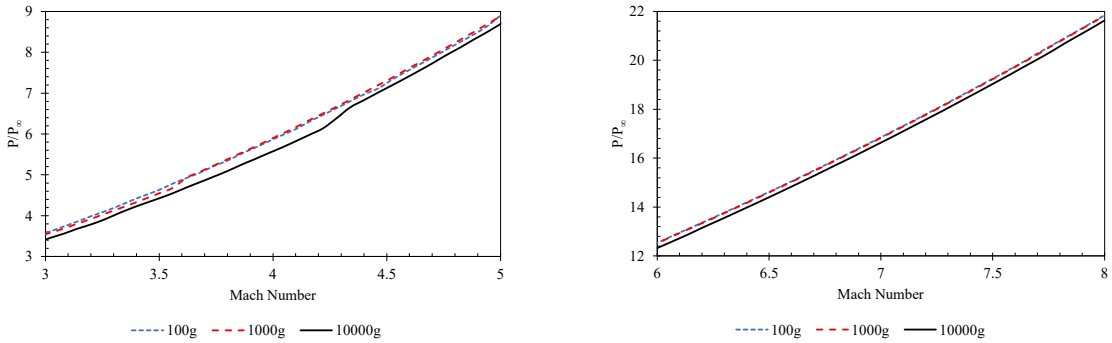

Figure 5. Dimensionless pressure coefficient of the blunt body during acceleration.

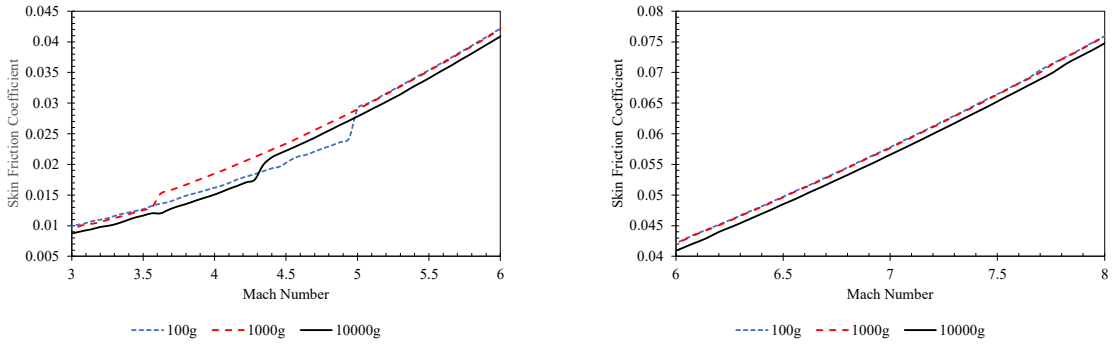

Figure 6. Skin friction coefficient of the blunt body during acceleration.

Similarly, Fig. 6 illustrates the comparison of the skin friction coefficient computed over the body at different Mach numbers for three acceleration magnitudes. It is observed that the start-up of the acceleration of the body has an impact on the wall shear stress distribution over the blunt body as the boundary of the shock wave starts to shrink, which directly affects the skin friction coefficient, for all three acceleration magnitudes. Beyond Mach = 5, the skin friction coefficients of the 100g and 1000g acceleration magnitudes are close to each other, whereas that of the 10000g magnitude is slightly lower than that of the other two cases.

The effect of decelerations on the dimensionless pressure of the blunt body is presented in Fig. 7. Similar to the acceleration cases, almost no difference is detected between the 100g and 1000g deceleration magnitude cases, and the pressure coefficient of the 10000g case is slightly higher than that of the other two cases. The effect of deceleration on the skin friction coefficient of the body is also demonstrated in Fig. 8. Likewise, the skin friction coefficient of the 10000g case is higher than that of the 100g and 1000g deceleration magnitude cases by 2.3% between M = 2 and M = 8. Unlike the acceleration, some variations in pressure and wall shear distribution at lower Mach numbers (see Fig. 5 (a) and Fig. 6 (a)) are not detected during deceleration. To further investigate the effects of acceleration and deceleration, the pressure coefficient distributions over the surface of the blunt body from the 10000g acceleration and deceleration magnitude cases at relatively low and high Mach numbers, M = 3 and M = 7, are compared and plotted in Fig. 9. It is seen that the nose of the blunt body (X/L = 0) experiences a relatively higher pressure at M = 3 when the body decelerates compared to the

opposite case. At M = 7, the pressure distribution over the spherical edge of the blunt body is similar between the two cases, but it tends to be slightly lower along the main body (0.32 < X/L < 1) when the body decelerates.

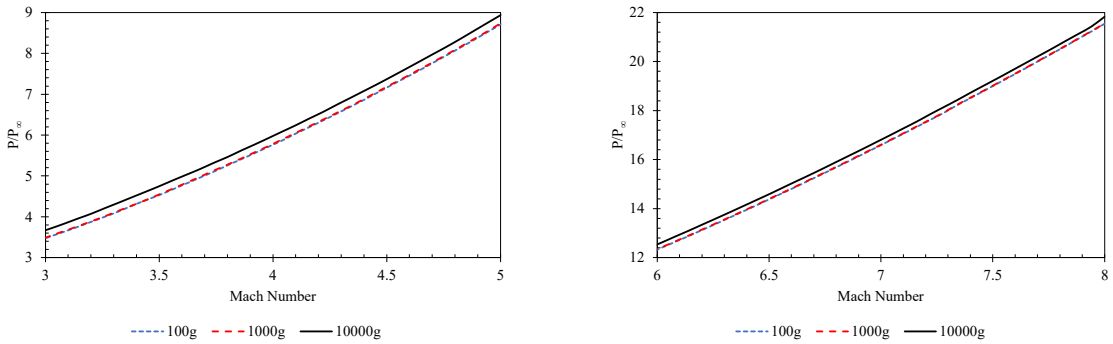

Figure 7. Dimensionless pressure coefficient of the blunt body during deceleration.

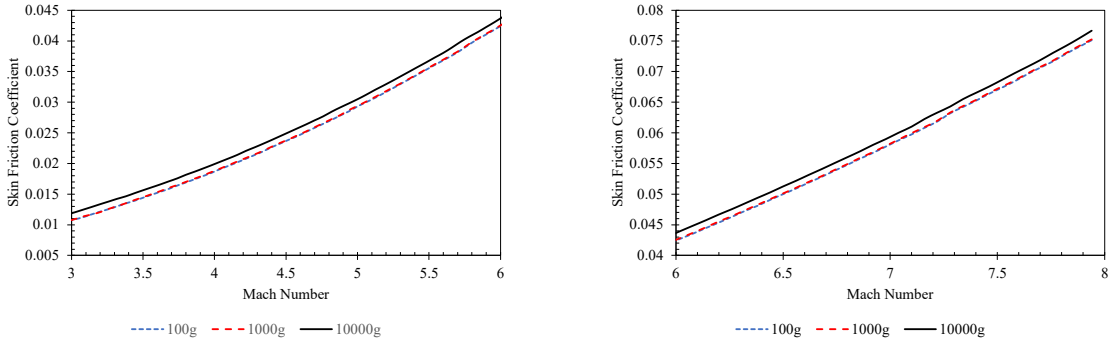

Figure 8. Skin friction coefficient of the blunt body during deceleration.

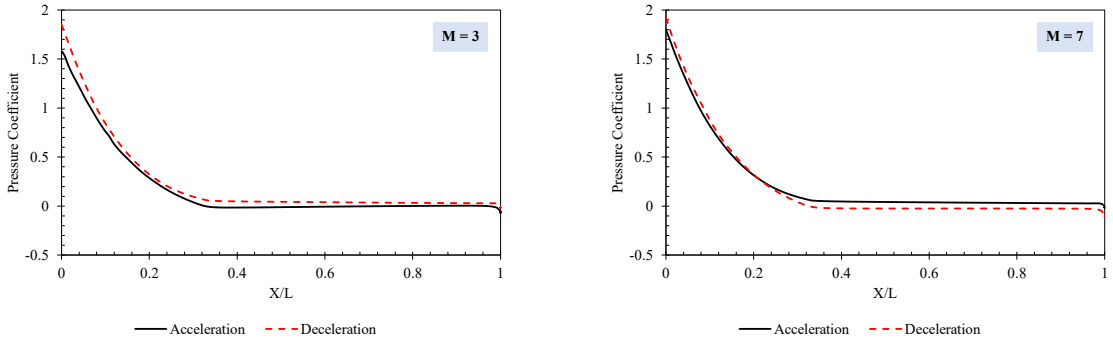

Figure 9. Pressure coefficient distribution over the blunt body during acceleration and deceleration.

The responses of the boundary layer and the shock wave to the acceleration are shown in Fig. 10. The dimensionless velocity (normalised by the freestream velocity) is plotted along the lines in the boundary layer in the aft region of the body and the shock wave at the nose of the body (the distances are normalised by the radius of the blunt body) for different Mach numbers in this figure. It is observed that the fluid velocity recovers more quickly in the boundary layer at low Mach numbers; however, only a slight difference is seen between M = 5 and M = 8 with the fluid velocity reaching approximately 80% of the freestream velocity. The responses of the shock wave can be seen in Fig. 10 (b). The boundary of the shock wave gets narrower as the body accelerates. The distance of the shock wave from the nose of the blunt body is 53% shorter at M = 5 and 56% shorter at M = 8 compared to M = 2. The fluid velocity is reduced by around 80% and 63% as it enters the shock wave zone at M = 5 & 8 and M = 2, respectively. Interesting behaviour is observed between M = 2 and M = 5 as the boundary of the shock wave starts to shrink due to acceleration. It is clearly seen that the dimensionless velocity within the shock wave at M = 3 is higher than that of the rest of the cases. This is due to some complications in velocity distribution around the stagnation point as the body accelerates. The dimensionless velocity profile of M = 3.5 tends to approach that of M = 5.

The effects of acceleration magnitude on the responses of the shock wave at M = 2, 3.5 and 5 are illustrated in Fig. 11. It can be seen that raising the acceleration magnitude from 100g to 10000g gradually reduces the fluid velocity as it goes further from the blunt body at M = 2 and 5. The effects of acceleration magnitude can be clearly observed at M = 3.5 as a great deviation in dimensionless velocity is detected within the boundary of the shock wave at different acceleration magnitudes. This agrees well with the variation in skin friction coefficient between M = 2 and M = 5, seen in Fig. 6. At M = 5, there is only a slight difference between different cases, which is also in agreement with Fig. 6.

Figure 12 highlights the effects of the oscillation of the body on the lift coefficient in one oscillation cycle at any Mach number during the acceleration or deceleration. It is shown that the lift coefficient is sinusoidal in relation to the frequency of the oscillation of the body, whereas the lift of the non-oscillating body remains almost zero over the entire oscillation cycle as no inflow angles are considered in this study.

Figures 13 and 14 demonstrate the dimensionless velocity (normalised by freestream velocity) and the pressure coefficient contours at M = 2, 5 and 8 during acceleration or deceleration. Since the velocity and pressure magnitudes depend on the Mach number, the dimensionless values are used for a direct comparison between different Mach numbers. As the flow fields at a specific Mach number during acceleration or deceleration are similar, one of them is only shown in this figure to make the paper more concise. At M = 2, the size of the shock wave is noticeably larger than the other two cases, and the velocity diverted from the blunt body is close to the freestream velocity. At M = 5 and M = 8, the flow fields around the blunt body are similar, but the size of the shock wave boundary is slightly larger in the former case. In terms of the pressure distribution, a significant difference is seen between the M = 2 case and the M = 5 and M = 8 cases. The pressure concentration around the stagnation point at the nose of the body is weaker at M = 2, due to a wider and larger shock wave, compared to the M = 5 and M = 8 cases.

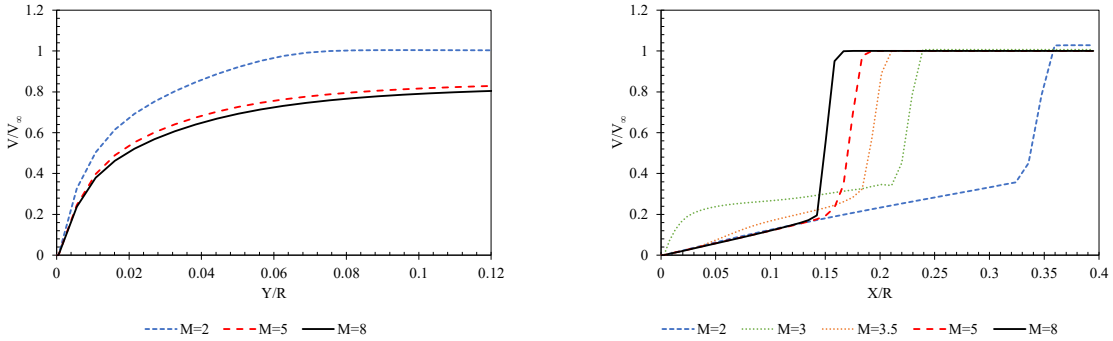

a) Boundary layer b) Shock wave

Figure 10. Responses of the boundary layer and the shock wave to acceleration.

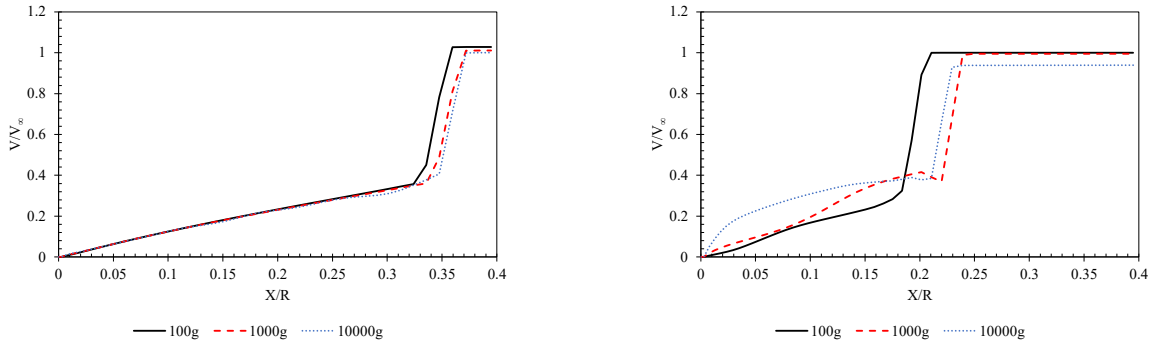

a) M = 2 b) M = 3.5

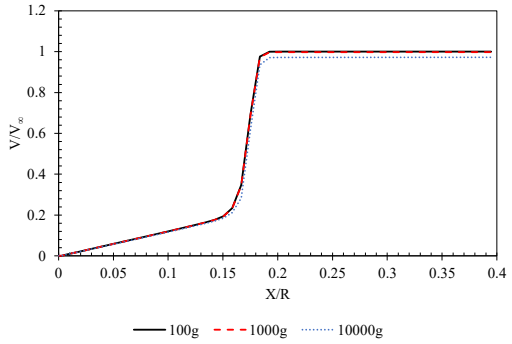

c) M = 5

Figure 11. Responses of the shock wave to different acceleration magnitudes.

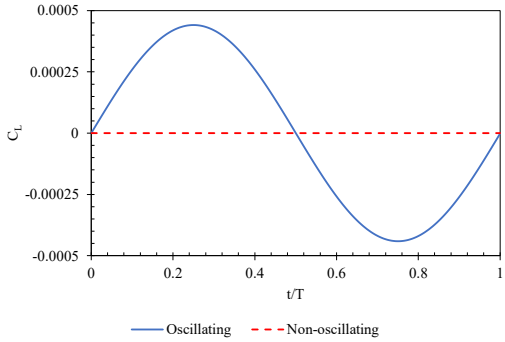

Figure 12. Lift coefficient variation of oscillating and non-oscillating blunt bodies.

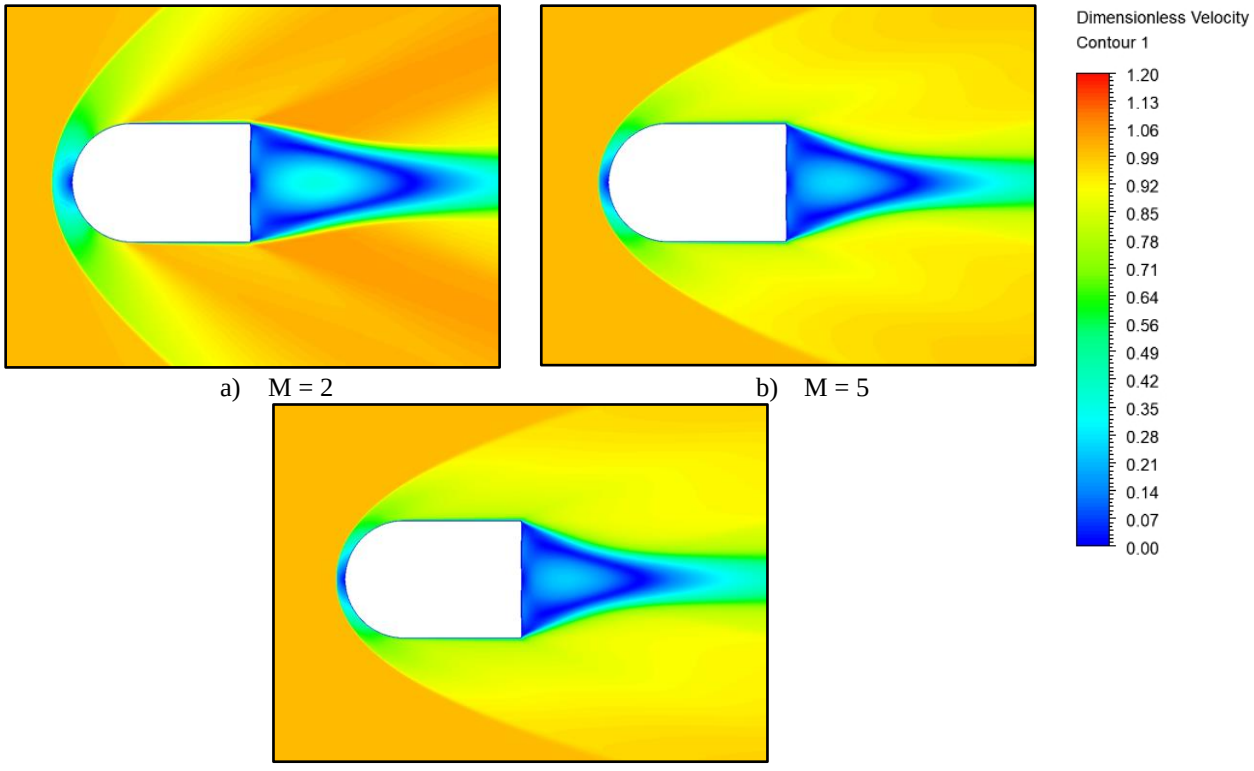

a) M = 2

b) M = 5

c) M = 8

Figure 13. Dimensionless velocity contours at different Mach numbers.

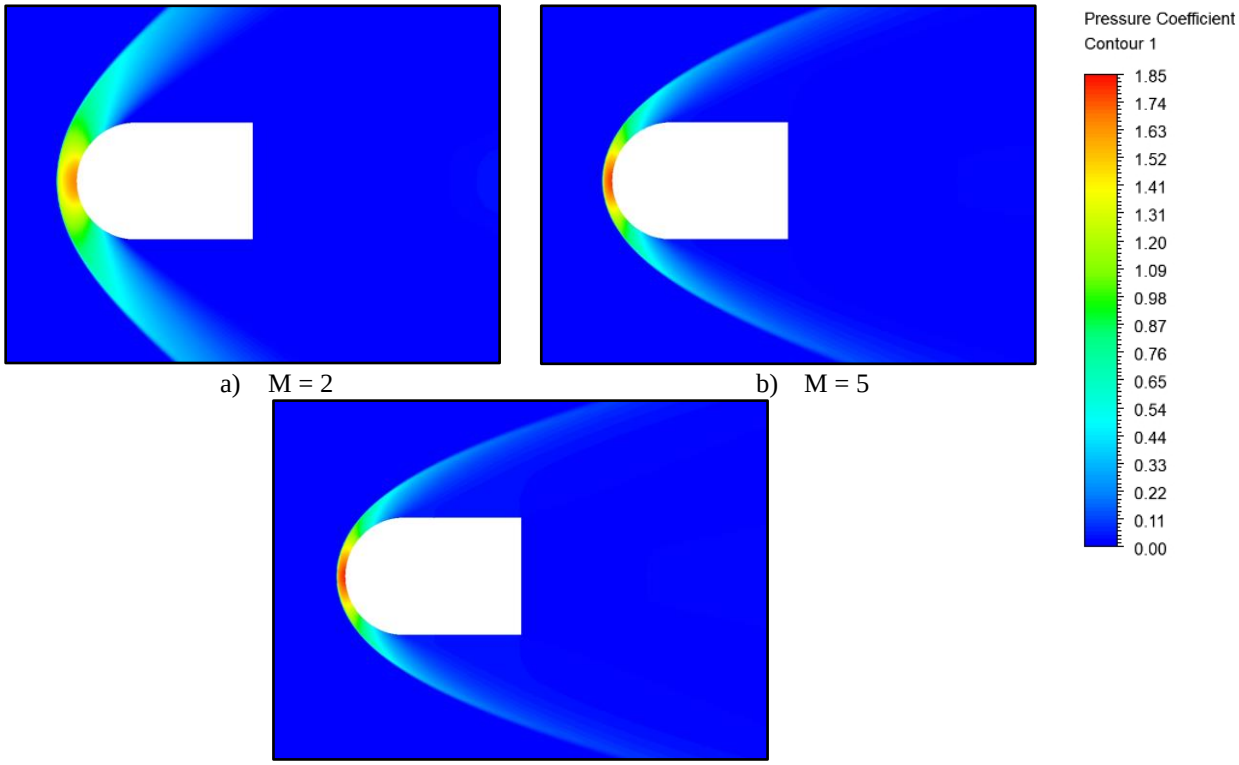

a) M = 2 b) M = 5

c) M = 8

Figure 14. Pressure coefficient contours at different Mach numbers.

4. CONCLUSIONS

This paper discusses the impact of acceleration and deceleration at different magnitudes on the aerodynamic performance of an oscillating blunt body, representing a leading edge of a wing aerofoil of a hypersonic aircraft. The aerodynamic characteristics such as pressure coefficient and skin friction coefficient during acceleration or deceleration at 100g and 1000g are close to each other while that of 10000g are slightly higher during deceleration and lower during acceleration. The differences are more pronounced at lower Mach numbers. Deviations in skin friction coefficient at different acceleration magnitudes are observed between M = 2 and M = 5, whereas these kinds of deviations are not observed during deceleration. It is also noted that the nose of the decelerating blunt body experiences a relatively higher-pressure distribution at lower Mach numbers in contrast to the accelerating body. In terms of the responses of the boundary layer and the shock wave, the fluid velocity recovers quickly in the boundary layer at low Mach numbers, whereas the boundary of the shock wave gets narrower as the body accelerates. The distance of the shock wave from the nose of the blunt body is 56% shorter at M = 8 than that of M = 2. The comparisons of the dimensionless velocity and pressure contours indicate that the fluid velocity relative to the freestream velocity is stronger within the boundary of the shock wave at M = 2 compared to higher Mach numbers, and the pressure concentration around the stagnation point is weaker at M = 2 in comparison to M = 5 and M = 8. It is also revealed that the sinusoidal distribution of the lift coefficient is observed due to the oscillation of the blunt body which has an influence on the aerodynamic force distribution over the blunt body.

5. REFERENCES

[1] Gledhill, I. M. A., Roohani, H., Forsberg, K., Eliasson, P., Skews, B. W., and Nordström, J., 2016, "Theoretical treatment of fluid flow for accelerating bodies," Theoretical and Computational Fluid Dynamics, 30(5), pp. 449-467.
[2] Zhou, D., Lu, Z., Guo, T., and Shen, E., 2018, "Development of a moving reference frame-based gas-kinetic BGK scheme for viscous flows around arbitrarily moving bodies," Journal of Computational Physics, 373, pp. 698-721.
[3] Raman, S. K., Kexin, W., Kim, T. H., Suryan, A., and Kim, H. D., 2020, "Effects of flap on the reentry aerodynamics of a blunt cone in the supersonic flow," International Journal of Mechanical Sciences, 176, p. 105396.
[4] Mahomed, I., Roohani, H., Skews, B. W., and Gledhill, I. M. A., 2022, "Unsteady shock wave dynamics in accelerating and decelerating flight," The Aeronautical Journal, 126(1296), pp. 401-423.
[5] Zhu, J., Shi, Z., Fu, J., and Chen, J., 2021, "Aerodynamic characteristics of hypersonic airfoils based on jet flow control technology," AIP Advances, 11(3), p. 035036.

[6] Gledhill, I. M. A., Forsberg, K., Eliasson, P., Baloyi, J., and Nordström, J., 2009, "Investigation of acceleration effects on missile aerodynamics using computational fluid dynamics," Aerospace Science and Technology, 13(4), pp. 197-203.
[7] Roohani, H., and Skews, B. W., 2009, "The influence of acceleration and deceleration on shock wave movement on and around aerofoils in transonic flight," Shock Waves, 19(4), pp. 297-305.
[8] Jiqiang, N., Yang, S., Qiujun, Y., Xiaoling, C., Yanping, Y., and Xiaofeng, Y., 2020, "Effect of acceleration and deceleration of a capsule train running at transonic speed on the flow and heat transfer in the tube," Aerospace Science and Technology, 105, p. 105977.
[9] Shirato, H., Maeta, K., Kato, Y., and Takasugi, Y., 2009, "Transient drag force on 2-D bluff bodies under gusty wind condition," 7th Asia-Pacific Conference on Wind Engineering, APCWE-VII.
[10] Yang, T., and Mason, M. S., 2019, "Aerodynamic characteristics of rectangular cylinders in steady and accelerating wind flow," Journal of Fluids and Structures, 90, pp. 246-262.
[11] SAWYER, R., and SULLIVAN, J., 1990, "Unsteady lift development on a constantly accelerated rectangular wing," 21st Fluid Dynamics, Plasma Dynamics and Lasers Conference.
[12] Sawyer, R. S., and Sullivan, J. P., 1991, "Lift development of delta wings undergoing constant acceleration from rest," Journal of Aircraft, 28(11), pp. 735-740.
[13] Roohani, H., 2011, "Aerodynamic effects of accelerating objects in air," University of the Witwatersrand.
[14] Win Naung, S., Rahmati, M., and Farokhi, H., 2021, "Direct Numerical Simulation of Interaction between Transient Flow and Blade Structure in a Modern Low-Pressure Turbine," International Journal of Mechanical Sciences, 192, p. 106104.
[15] Win Naung, S., Nakhchi, M. E., and Rahmati, M., 2021, "Prediction of flutter effects on transient flow structure and aeroelasticity of low-pressure turbine cascade using direct numerical simulations," Aerospace Science and Technology, 119, p. 107151.
[16] Steijl, R., and Barakos, G., 2008, "Sliding mesh algorithm for CFD analysis of helicopter rotor–fuselage aerodynamics," International Journal for Numerical Methods in Fluids, 58(5), pp. 527-549.
[17] Inoue, O., Sakai, T., and Nishida, M., 1997, "Focusing shock waves generated by an accelerating projectile," Fluid Dynamics Research, 21(6), pp. 403-416.
[18] Marquart, J. E., and Eastep, F. E., 1998, "Numerical Representation of Pitching and Nonpitching Airfoils Undergoing Linear Acceleration," Journal of Aircraft, 35(5), pp. 761-768.
[19] Saito, T., Hatanaka, K., Yamashita, H., Ogawa, T., Obayashi, S., and Takayama, K., 2011, "Shock stand-off distance of a solid sphere decelerating in transonic velocity range," Shock Waves, 21(5), pp. 483-489.
[20] Li, L., Sherwin, S. J., and Bearman, P. W., 2002, "A moving frame of reference algorithm for fluid/structure interaction of rotating and translating bodies," International Journal for Numerical Methods in Fluids, 38(2), pp. 187-206.
[21] Kageyama, A., and Hyodo, M., 2006, "Eulerian derivation of the Coriolis force," Geochemistry, Geophysics, Geosystems, 7(2).
[22] Manjarres, D. A., Herrera, W. J., and Diaz, R. A., 2013, "Work and energy in rotating systems," American Journal of Physics, 81(8), pp. 597-602.
[23] Cariglino, F., Ceresola, N., and Arina, R., 2014, "External Aerodynamics Simulations in a Rotating Frame of Reference," International Journal of Aerospace Engineering, 2014, p. 654037.
[24] Kim, D., and Choi, H., 2006, "Immersed boundary method for flow around an arbitrarily moving body," Journal of Computational Physics, 212(2), pp. 662-680.
[25] Combrinck, M. L., Dala, L. N., and Lipatov, I. I., "Boundary layer response to arbitrary acceleration."
[26] Win Naung, S., Nakhchi, M. E., and Rahmati, M., 2021, "High-fidelity CFD simulations of two wind turbines in arrays using nonlinear frequency domain solution method," Renewable Energy, 174, pp. 984-1005.
[27] Win Naung, S., Rahmati, M., and Farokhi, H., 2021, "Aeromechanical Analysis of a Complete Wind Turbine Using Nonlinear Frequency Domain Solution Method," Journal of Engineering for Gas Turbines and Power, 143(1), p. 011018.
[28] Win Naung, S., Rahmati, M., and Farokhi, H., 2021, "Nonlinear frequency domain solution method for aerodynamic and aeromechanical analysis of wind turbines," Renewable Energy, 167, pp. 66-81.
[29] HOLDEN, M., MOSELLE, J., WIETING, A., and GLASS, C., 1988, "Studies of aerothermal loads generated in regions of shock/shock interaction in hypersonic flow," 26th Aerospace Sciences Meeting.
[30] Cao, C., Nie, C., Pan, S., Cai, J., and Qu, K., 2019, "A constrained reduced-order method for fast prediction of steady hypersonic flows," Aerospace Science and Technology, 91, pp. 679-690.